MODELING OF ACOUSTICALLY TREATED NACELLE LIP TRANSPIRATION FLOW ANTI-ICING SYSTEM

R. Elangovan†, R. F. Olsen† and N. D. Reynolds‡
†The Boeing Company, Seattle, Washington 98124, USA., ‡Department of Geology, Wichita State University, Wichita, Kansas, USA

Keywords: transpiration flow anti-icing system, nacelle lip acoustic treatment, laser drilled acoustic panel, transpiration flow heat transfer coefficient, ADI method

Abstract

Acoustically treated nacelle lip transpiration flow anti-icing system is analyzed by solving the two dimensional transient heat conduction equation with a combined transpiration flow convective heat transfer and thermodynamics energy transfer rate boundary condition. The nacelle lip skin surface temperature distribution is determined when the skin exposed to airflow laden with atmospheric cloud super cooled water droplets of known size distribution is heated using transpiration air flow.

Nomenclature

c	specific heat of Titanium face sheet, $Btu/lbm.F$ $[J/kg.K]$
c_p	specific heat of air, $Btu/lbm.F$ $[J/kg.K]$
h	surface convection heat transfer coefficient, $Btu/h.ft^2.R$ $[W/m^2.K]$
k	thermal conductivity of air, $Btu/h.ft.^\circ F$ $[W/m.K]$
LWC	Cloud liquid water content, g/m^3
M	Mach number
n, y	axis normal to the surface
Pr	Prandtl number of air
q	heat balance at the surface, $Btu/h.ft^2$ $[W/m^2]$
s, x	axis along the surface
St	Transpiring Stanton number
T	temperature, R $[K]$
U_e	boundary layer edge velocity, ft/s $[m/s]$
v_t	transpiration flow velocity, ft/s $[m/s]$
W_{ENG}	Inlet mass flow, lbm/s $[kg/s]$
Re_s	Reynolds number of air
St_N	Non-transpiring Stanton number
∞	freestream
e	boundary layer edge
$evap$	water evaporation
frz	water freezing
i	face sheet inner surface
imp	water impingement
l	lip lower edge
o	face sheet outer surface
r	lip upper edge
run	water runback
β	local collection efficiency
κ	face sheet material thermal conductivity, $Btu/h.ft.^\circ F$ $[W/m.K]$
ρ	density of air, lbm/ft^3 $[kg/m^3]$
ρ_m	density of face sheet, lbm/ft^3 $[kg/m^3]$
τ	time, s

1 Introduction

The acoustic liner forms the inner wall surface of the engine nacelle (inlet) and the liner is made of perforated face sheet, solid back sheet, and honey comb sandwich core with septum to suppress the fan noise. The present day engine inlet lip surface does not have acoustic treatment. Further reduction in fan noise can be achieved by providing acoustic treatment to the inlet lip surface.

The motivation behind the anti-ice lip surface acoustic treatment is based on the need for more

noise reduction to meet current and future anticipated noise rules for certification and/or local airport noise restrictions [12, 13, 14, 15, 16]. Over 200 airports currently have noise curfews which are impacting flight operations and are limiting airport growth capacity. A prominent few of the more than 200 airports are identified here along with the nature of their curfew.

- London Heathrow/Gatwick/Stansted QC-based curfews
- Madrid Barajas nighttime runway-use restrictions
- Paris Orly Airport nighttime ban
- Burbank Airport voluntary nighttime ban
- Osaka Airport nighttime ban

Nighttime bans on flight operations can significantly impact growth and limit the number of potential flight operations. Long range flights have an added complexity relative to available operational windows of the two airports involved. A nighttime ban at one airport will place a definite departure window at the airport of origin depending on the distance and time zone. Over 25 airports have quotas limiting flight operations and airport growth capacity. Five of the prominent airports having these quotas are listed below.

- London Heathrow/Gatwick/Stansted QC System
- Brussels Charleroi Airport QC System
- Munich Airport nighttime movement limits
- Sydney Kingsford Smith Airport nighttime movement limits
- Copenhagen Airport annual total movement limit

QC system refers to the ***Quota Count*** system originally developed for London area airports (Heathrow, Gatwick, and Stansted airports)[12]. The QC system was initially designed to limit and control noise emissions that occur at night. This system, since it is a quota system, is also reducing daytime noise exposure due to airplane flight operations.

The Piccolo jet and the Nozzle type bleed air anti-icing systems, currently utilized in commercial airplanes, will not be suitable for anti-icing the lip acoustic liner due to the excessive bleed air requirements to maintain the thick air filled liner face sheet above freezing temperature. The transpiration flow anti-icing system is being considered for anti-icing the acoustically treated lip. The system has been successfully tested in the icing tunnel and flight test preparations are underway.

The analysis method developed using the alternating direction implicit (ADI) scheme [1, 18] for evaluating the performance of the Low Power Electric De-Icing System [7] and the Piccolo Tube Jet Impingement Thermal Anti-Icing System [6] has been extended to the analysis of transpiration flow anti-icing system.

2 Pneumatic Transpiration Flow Anti-Icing System

2.1 Helmholtz Resonator Acoustic Panel

The Boeing Company is developing technology to apply sound absorbing liners on the engine nacelle inlet lip surface area [8, 21, 10]. The liners of interest for this application are of the Helmholtz resonator type similar to those currently used for the nacelle inlet diffuser wall surface and fan exhaust duct. One of many technical challenges in treating the nacelle lip surface with acoustic panels is to provide ice and rain protection.

The Helmholtz resonator acoustic panel construction for nacelle applications is typically a honeycomb sandwich configuration involving a perforated or porous face sheet and an impervious backing sheet as shown on Fig. 1. The walls of the honeycomb structure form a multitude of individual resonating chambers which can react with the acoustic field within the duct.

2.2 Current Nacelle Anti-Icing Systems

All of the current Boeing nacelle anti-ice systems utilize hot engine bleed air from the engines' high pressure compressor bleed ports for the anti-ice

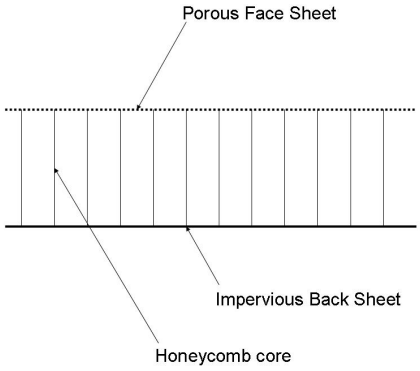

Fig. 1 Helmholtz resonator acoustic panel construction

heat source. This high pressure air is directed to a chamber or cavity located in the region of the nacelle lip area of the inlet. The nose cavity at the lip is defined by the lip aerodynamic geometry (flow surface) and a forward structural bulkhead. This cavity is typically referred to as the "D" duct (Fig. 2) and is heated with engine hot bleed air to provide ice and rain protection for the nacelle.

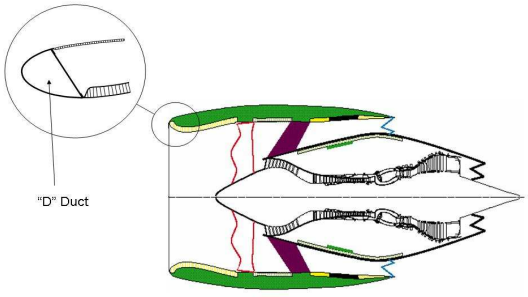

Fig. 2 Nacelle lip "D" duct anti-ice treatment

One of the problems in applying the acoustic panel to the lip region of the nacelle is with the ability to conduct the necessary heat to the flow surface at the porous face sheet. The relatively still air within the resonator chambers behaves like an insulation barrier to the heat flow from the impervious back skin. The relatively thin wall construction of the honeycomb core does not provide a sufficient conduction path to transmit the necessary heat to the porous face sheet for anti-ice purposes.

2.3 Transpiration Flow Anti-Icing System

The solution to the heat transfer problem that is presented here is to utilize transpiration flow of hot bleed air through the acoustic panel to the porous face sheet. A number of patents have been issued based on the general concept of transpiration airflow heating [3, 4, 5, 17]. Figures (3, 4, and 5) show the general concept and arrangement for the transpiration flow acoustic panel. The acoustic panel designed for transpiration flow, illustrated on Fig. 3, is shaped to become the aerodynamic contour of the nacelle lip as shown on Fig. 4. The porous face sheet becomes the aerodynamic flow surface of the lip and the "slightly" porous back sheet faces the interior of the "D" duct. Fig. 5 completes the concept arrangement with the addition of plumbing to supply hot bleed air from the engine's compressor bleed port to the nacelle inlet "D" duct compartment. Flow restrictors and pressure regulating control valves are required to supply the appropriate mass flow and pressure to the "D"

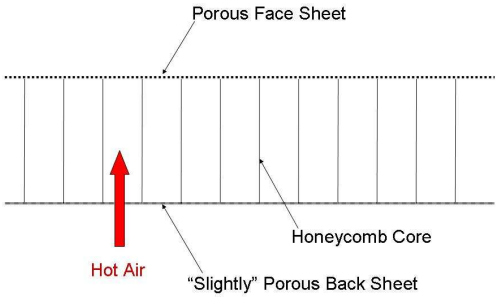

Fig. 3 Transpiration flow through acoustic panel

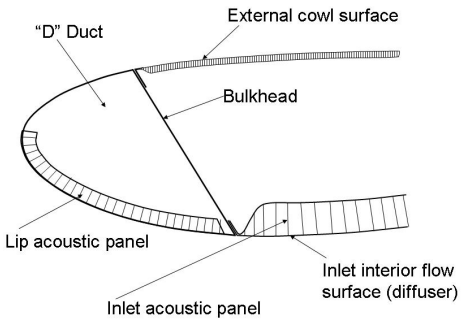

Fig. 4 Nacelle inlet lip configuration with acoustic panel

Fig. 6 Rolls Royce Trent 800 advanced acoustic inlet equipped with acoustically treated lip with transpiration anti-ice system

duct cavity. The photo shown on Fig. 6 is an ex-

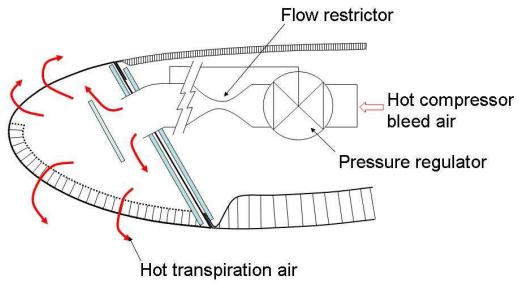

Fig. 5 Nacelle lip transpiration flow anti-ice system with acoustic panel

perimental inlet equipped with a functional transpiration anti-ice concept applied to the nacelle lip of a Trent 800 engine nacelle inlet. The Trent 800 engine is used on models of the 777 airplane.

2.4 Design and Manufacturing Considerations

One of the design considerations for the transpiration lip concept is with selecting the target operating pressure for the "D" duct cavity. The surface pressure distribution along the surface of the lip is a function of the lip geometry, the engine power setting, and the forward speed of the airplane. For static or ground operations, the surface pressures are always negative relative to ambient conditions such that any pressure in the "D" duct results in transpiration flow from the "D" duct cavity to the external flow field. With forward speed of the airplane, this picture changes and it is now possible to have a stagnation point on the inlet lip which will be a function of the forward speed and the engine power setting. This will produce a local area of higher pressure on the surface that must be overcome to result in transpiration flow from the "D" duct to the external surface. Otherwise, external flow will now enter the "D" duct. At higher speeds, like 0.9 Mach, these pressures will be significant and will consequently require an appropriate delta pressure gradient as shown on Fig. 7 to ensure that the required mass and heat flow are achieved.

The development of this application is as much about manufacturing methods, material selection, and processes as it is about acoustics and ice and rain protection. For this application, LASER drilling was selected as the method for creating the porous face sheet and backing sheets.

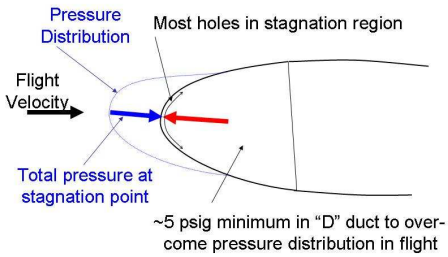

Fig. 7 Operating pressure considerations for transpiration flow

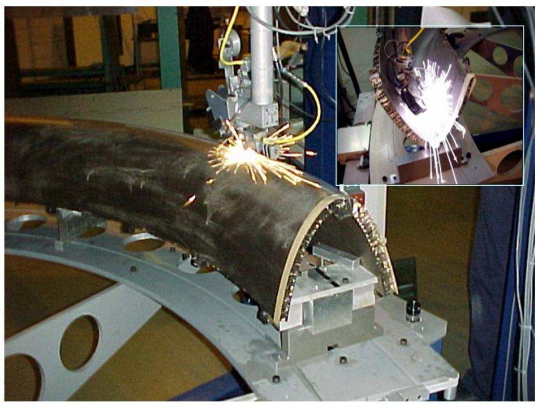

Fig. 8 Laser drilling of lip face sheet and back sheet

Titanium was selected for the lip materials over aluminum because of the relative ease in LASER drilling Ti compared with Al. The technology for laser drilling Al is not sufficiently mature enough today to use Al. Normally Al would be preferred because of the much higher thermal conductivity relative to Ti. The forming and welding of Ti honeycomb core face and backing sheets all required their own development programs.

Laser drilling was selected as the means for perforating the face sheet and backing sheets of the transpiration flow lip. Fig. 8 is a photo of the actual Laser drilling taking place on quadrants of the Trent800 Advanced Acoustic Inlet. CAV Aerospace, formerly known as AS&T (Aerospace Systems & Technologies, $http://www.weepingwings.com/$) developed the technologies for drilling the holes on the completed lip skins of the inlet lip. The Advanced Acoustic Inlet required about 21 million holes.

The thermal analysis codes of this paper were an essential element of the design and development process to size the open areas for the face and backing sheets to work with the regulated temperatures and pressures of the hot bleed air system.

2.5 Icing Tunnel Model and Testing

Key elements of the transpiration lip concept were evaluated in icing tunnel simulations. These tests were used to establish important empirical coefficients supporting the thermal analysis models such as the ever elusive film coefficients under various transpiration flow rates. A photo of the 4 foot wide test model lip that was tested in the Boeing Research Aerodynamics Icing Tunnel (BRAIT) is shown on Fig. 9. In the photo, a close up of the acoustic panel is shown. A light source was placed behind the panel to illuminate the LASER drilled holes in the face sheet. The blockage from the weld between the face sheet and core can also be seen as the core geometry pattern. The two photos and thermal picture shown on Fig. 10 is that of the model situated in the Icing tunnel. Although the inlet lip is a round aerodynamic structure, the model simulation in the icing tunnel is kept as a straight section like a wing leading edge. This allowed the experiment to use a full scale profile of the leading edge lip surface in the simulation. All of the relevant in-flight icing conditions can be simulated in this way. Part of the icing tunnel test evaluations included simulations of bug splatter contaminations. Tests indicated that the combination of heat and the transpiration flow actually cleared any blockages from bug impingement and was

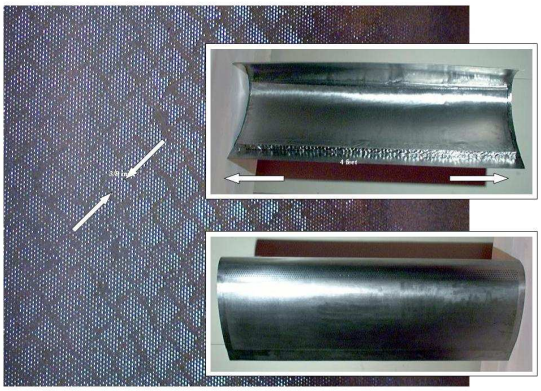

Fig. 9 Transpiration lip icing tunnel test model

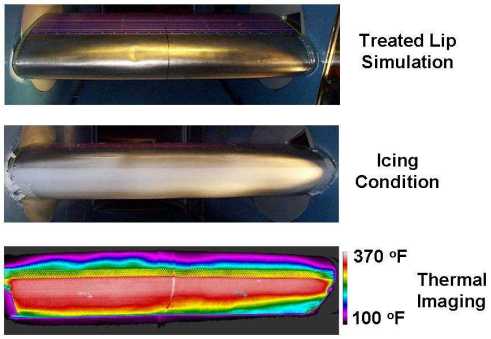

Fig. 10 Icing tunnel transpiration flow anti-icing test

not viewed as a problem with this concept.

3 Heat Conduction Equation

The two-dimensional time dependent heat conduction equation, in the surface coordinate system shown on Fig. 11, can be written as

$$\rho_m c \frac{\partial T}{\partial \tau} = \frac{\partial}{\partial n}\left(\kappa_n \frac{\partial T}{\partial n}\right) + \frac{\partial}{\partial s}\left(\kappa_s \frac{\partial T}{\partial s}\right) \qquad (1)$$

Using alternating direction implicit (ADI) scheme, the face sheet surface temperature distribution is determined by solving the finite difference approximation of Eq. 1 with the boundary conditions [7, 6].

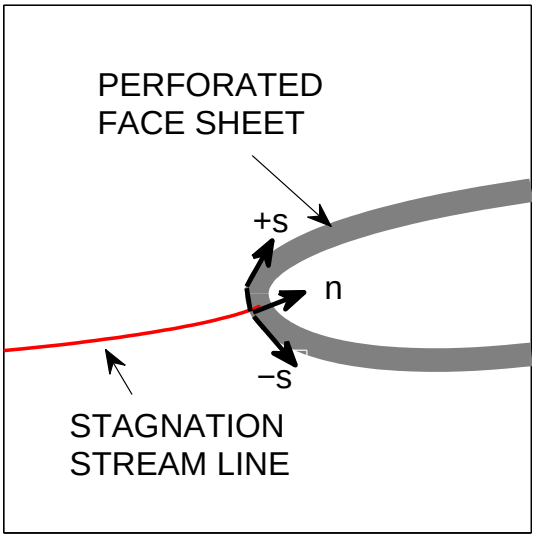

Fig. 11 Coordinate system

3.1 Boundary Conditions

The heat transfer rate at the face sheet outer and inner surface (Fig. 12) are given by

$$-\kappa_m \frac{\partial T}{\partial y}\bigg|_{y=0} = h_o\,(T_e - T_o) + q(\tau) \qquad (2)$$

and

$$-\kappa_m \frac{\partial T}{\partial y}\bigg|_{y=t} = h_i\,(T_i - T_p) \qquad (3)$$

respectively.

In Eqs. 2 and 3, q is the thermodynamic energy transfer rate at the surface, h_o is the transpiration flow convective heat transfer coefficient at the outer surface, and h_i is the transpiration flow convective heat transfer coefficient at the inner surface A number of semi empirical heat transfer correlations, for the non-traspiring convective heat transfer coefficient over airfoil surface, are available in the literature [2, 20]. The transpiring convective heat transfer coefficient for the outer surface is obtained from the non-transpiring

Stanton number as described in the following section.

The lip upper and lower edges of the skin are located outside the heated area. Therefore, the temperatures at these locations can be assumed to be at the corresponding local static ambient temperatures, i.e., $T_u = T_r$ and $T_l = T_l$.

3.2 Transpiration Flow Convection Heat Transfer Coefficients

The heat exchange effectiveness of perforated surface with transpiring airflow was measured in the laboratory by Japanese researchers [9]. Besides a discussion of the experimental results, they presented a simple theory for determining an expression for the transpiring Stanton number based on a balance between heat transfer by conduction through the perforated plate and heat transfer by convection due to air passing through the plate. The external heat transfer coefficient, h_o, in the presence of transpiration is calculated from the Stanton number of the transpiring flow. The procedure for determining the transpiring Stanton number, St, is described below.

The energy balance through the face sheet shown on Fig. 12 gives

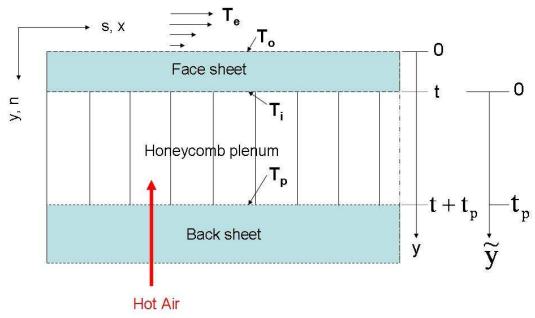

Fig. 12 Model for the derivation of transpiration flow convection heat transfer coefficient

$$(\rho c_p v_t)_1 \frac{dT}{dy} = \kappa \frac{d^2T}{dy^2},\ 0 \le y \le t. \qquad (4)$$

The solution of Eq. 4 is

$$T(y) = T_o + \frac{c_1}{b_1}\left(1 - e^{-b_1 y}\right) \qquad (5)$$

where,

$$b_1 = \frac{(\rho c_p v_t)_1}{\kappa} \text{ and } c_1 = b_1 \frac{T_i - T_o}{1 - e^{-b_1 t}} \qquad (6)$$

The heat transfer rate at the outer, q_o, and inner, q_i, surface of the face sheet are given by

$$q_o = (\rho c_p v_t)_1 \frac{T_i - T_o}{1 - e^{-b_1 t}} \text{ and } q_1 = q_o e^{-b_1 t} \qquad (7)$$

From Eq. 7 the temperature difference between inner and outer surface of face sheet is

$$T_i - T_o = \frac{q_o}{(\rho c_p v_t)_1}\left(1 - e^{-b_1 t}\right) \qquad (8)$$

By definition the temperature difference between the face sheet outer surface and boundary layer edge is

$$T_o - T_e = \frac{q_o}{h_o} \qquad (9)$$

Similarly, the energy balance equation for the honeycomb plenum air region of Fig. 12 is given by

$$(\rho c_p v_t)_2 \frac{dT}{d\tilde{y}} = k \frac{d^2T}{d\tilde{y}^2},\ \tilde{y} = y - t,\ 0 \le \tilde{y} \le t_p \qquad (10)$$

and the solution of Eq. 10 is given by

$$T(\tilde{y}) = T_i + \frac{c_2}{b_2}\left(1 - e^{-b_2 \tilde{y}}\right) \qquad (11)$$

where,

$$b_2 = \frac{(\rho c_p v_t)_2}{k} \text{ and } c_2 = b_2 \frac{T_p - T_i}{1 - e^{-b_2 t_p}} \qquad (12)$$

The heat transfer rate, q_i, at the inner surface of the face sheet is

$$q_i = (\rho c_p v_t)_2 \frac{T_p - T_i}{1 - e^{-b_2 t_p}} = h_i (T_p - T_i) \qquad (13)$$

Therefore, the face sheet inner surface heat transfer coefficient is given by

$$\begin{aligned} h_i &= \frac{(\rho c_p v_t)_2}{1 - e^{-b_2 t_p}} \\ &\approx (\rho c_p v_t)_2, \text{ since } e^{b_2 t_p} \gg 1. \end{aligned} \qquad (14)$$

At $y = t$,

$$(\rho c_p v_t)_2 = (\rho c_p v_t)_1 \tag{15}$$

Using Eqs. 7 and 15 the temperature difference between plenum and face sheet inner surface can be written as

$$T_p - T_i = \frac{q_i}{h_i} = \frac{q_o e^{-b_1 t}}{(\rho c_p v_t)_2} = \frac{q_o e^{-b_1 t}}{(\rho c_p v_t)_1} \tag{16}$$

The transpiration thermal effectiveness, η, is defined as

$$\eta = \frac{T_o - T_e}{T_p - T_e} = \frac{T_o - T_e}{T_p - T_i + T_i - T_o + T_o - T_e} \tag{17}$$

The transpiration ratio, F, and the transpiring Stanton number, St, are defined as

$$F = \frac{(\rho c_p v_t)_2}{(\rho c_p U)_e} \tag{18}$$

$$St = \frac{h_o}{(\rho c_p U)_e} \tag{19}$$

Substituting Eqs. 8, 9, and 16 in Eq. 17 and simplifying,

$$\eta = \frac{1}{1 + \frac{h_o}{(\rho c_p v_t)_2}} = \frac{1}{1 + \frac{St}{F}} \tag{20}$$

From Eq. 20 the transpiring Stanton number and face sheet outer surface heat transfer coefficient are obtained as

$$St(s) = \frac{F}{\eta}(1 - \eta) \tag{21}$$

$$h_o = 3600 \rho_e c_{pe} U_e St \tag{22}$$

The expression for transpiration thermal effectiveness, found by the Reference [9] researchers, is

$$\eta(s) = 1 - e^{-\frac{F}{St_N}} \tag{23}$$

where, St_N is the non-transpiring Stanton number. For turbulent flow over flat plate

$$St_N = 0.029 Re_s^{-0.2} Pr^{-\frac{2}{3}} \tag{24}$$

The face sheet external and internal transpiring heat transfer coefficients, required by the boundary condition Eqs. 2 and 3, are Eqs. 22 and 14. The external convection heat transfer coefficient with transpiration is lower than the solid wall non-transpiring convection heat transfer coefficient and therefore a reduction in the bleed air requirement to anti-ice the surface is achieved.

3.3 Thermodynamic Energy Transfer

In the boundary condition Eq. 2 the heat transfer at the external surface is divided into two parts, turbulent boundary layer heat transfer rate and energy transfer rate due to impinging water droplets. In the energy transfer rate calculation, taking into account the phase change taking place, the mass and energy balance of the water collected on the surface is performed. The free stream air velocity, boundary layer edge velocity, atmospheric cloud liquid water content, LWC, and the local collection efficiency at the inlet lip surface, β, obtained from droplet trajectory analysis computer program are required for the energy transfer rate calculation.

The thermodynamic energy transfer rate at the external surface, q, required in the boundary condition Eq. 2 is given by

$$q(\tau) = q_{imp} + q_{run} + q_{frz} - q_{evap} \tag{25}$$

where, q_{imp} represents the heat gain at the surface due to the kinetic energy of the impinging water particles minus the heat loss at the surface due to the warming of the impinging water; q_{run} is the heat gain at the surface due to water runback; q_{frz} is the heat gain due to water freezing on the surface; and q_{evap} is the heat loss due to evaporation.

Detailed derivation of expressions for the water impingement, water runback, water freezing, and water evaporation components of the energy transfer rate equation are presented in References[7, 6, 2, 20, 11, 19].

4 Analysis of Engine Inlet

The transpiration flow anti-icing system analysis computer program requires the following data files: 1) the geometry coordinate data file describing the geometry; 2) the boundary layer edge surface velocity data file; 3) the atmospheric cloud water droplet local collection efficiency data file; and 4) the transpiration flow rate data file.

4.1 Geometry and Analysis Condition

The geometry selected for analysis is the Rolls Royce Trent 800 engine inlet shown on Fig. 13. The flight and anti-icing conditions selected for analyses are shown in Tables 1 and 2. The tables show that the transpiration air flow supply pressures in the D-duct are regulated to 5 psig above ambient pressure.

Table 1 FLIGHT CONDITIONS

$Altitude$ (ft)	M_∞	p_∞ $(psia)$	T_∞ $(^\circ F)$	W_{ENG} (Lbm/sec)
15000	0.450	8.29	0	1170.9
15000	0.450	8.29	0	1170.9

Table 2 ANTI-ICING CONDITIONS

T_{amb} $(^\circ F)$	P_{Bleed} $(psia)$	T_{Bleed} $(^\circ F)$	LWC $(\frac{g}{m^3})$
21	13.29	565	0.52
-22	13.29	490	0.14

4.2 Flow Field Analysis

Using an in-house computational fluid dynamics (CFD) computer program the flow field analysis of the inlet at the specified flight conditions and engine mass flow rate was performed. The flow field data in the form of streamline traces are shown on Fig. 13. The boundary layer edge surface velocity data is shown on Fig. 14.

4.3 Trajectory Analysis

The input data for the trajectory analysis computer program is the geometry file, the flow field file from the CFD program, and the atmospheric cloud droplet size distribution, such as Langmuir-D distribution. For the droplet diameters specified by the size distribution, the trajectory program computes the droplet trajectories that impinge on the inlet and calculates the local collection efficiency. The local collection efficiency data is shown on Fig. 15. The local water collection efficiency, β, at a point on the body surface is defined as the impinging droplet stream tube free stream area perpendicular to the free stream divided by the corresponding impinging area on the body surface.

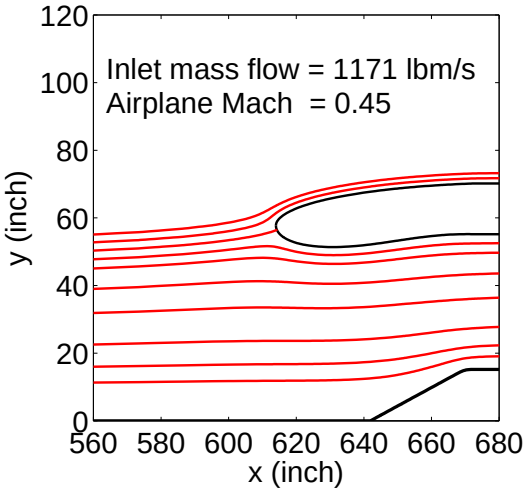

Fig. 13 Inlet lip flow field streamlines

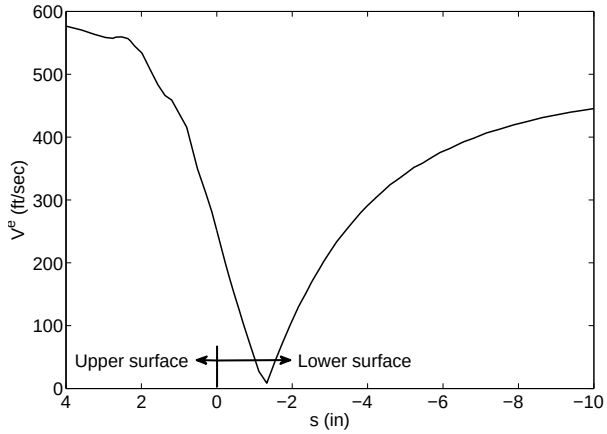

Fig. 14 Inlet lip boundary layer edge velocity as function of surface distance from highlight

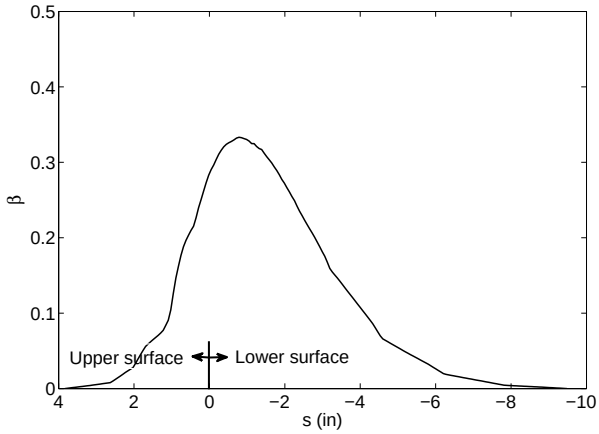

Fig. 15 Inlet lip local collection efficiency as function of surface distance from highlight

4.4 Transpiration Flow Network Analysis

The face sheet surface pressure distribution obtained from the CFD program and the specified bleed air supply pressure (5 psig) and temperature at the back sheet are the boundary conditions for flow network analysis. The face sheet used in this analysis is 32 mil thick titanium and consists of two different percent open area (poa) regions namely, the upper surface region above the highlight and the lower surface region below the highlight. The laser drilled holes diameter for both regions are 0.004 inch. The poa for the lower surface is 4.0 and for the upper surface is 2.0. The poa for the face sheet lower surface region was arrived at based on noise suppression considerations. The poa for the upper surface was the minimum that would give adequate heat transfer for anti-ice.

The back sheet used in this analysis is 50 mil thick titanium and consists of three different poa regions. The laser drilled hole diameters for the three regions are 0.002 inch. The poa for the lower region is 0.13, for the highlight region is 0.20, and for the upper region is 0.12. The poa's for the back sheet were arrived at based on anti-icing airflow requirements for the three regions.

The face sheet and back sheet pressure drop coefficient data required for the flow network analysis program were determined using acoustic laboratory Flow Bench apparatus. The computed transpiration flow rate data for the acoustic panel is shown on Fig. 16.

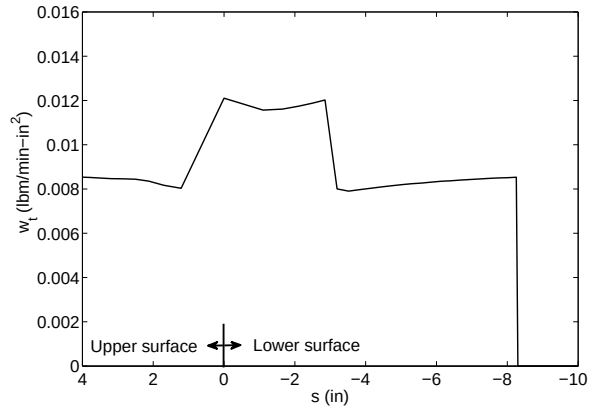

Fig. 16 Transpiration flow rate as function of surface distance from highlight

5 Anti-Icing Analysis of Engine Inlet Lip

Anti-icing analysis of Rolls Royce Trent 800 engine inlet was performed at two anti-icing conditions (Table 2). The anti-icing surface (face sheet) material property data required for analysis are shown in Table 3.

Table 3 FACE SHEET MATERIAL PROPERTY

κ_n $(\frac{Btu}{h\ ft\ ^\circ F})$	κ_s $(\frac{Btu}{h\ ft\ ^\circ F})$	ρ $(\frac{lbm}{ft^3})$	c $(\frac{Btu}{lbm\ ^\circ F})$	$thick$ (in)
12.65	12.65	283.39	0.13	0.032

The analysis result for $21^\circ F$ ambient temperature, and $565^\circ F$ bleed air temperature (case-1) for dry $(LWC = 0)$ condition and wet $(LWC = 0.52)$ condition are shown on Fig. 17. The results show as expected the skin temperature for wet condition is lower than the dry condition due to evaporation of water impinging on the surface. For the wet condition, near the stagnation point

region a slightly higher skin temperature is observed. This can attributed to the fact that the specified transpiration flow rate at the stagnation point region is higher and therefore the face sheet inner surface heat transfer coefficient is higher and the outer surface transpiring heat transfer coefficient is lower. Next to the stagnation region, due to both runback water and impinging water evaporation, a flat dip in the skin temperature is observed. In the lower surface close to 8 inch from the highlight a higher surface temperature peak is observed. This is due to the fact that in this region water collection efficiency is negligible and also water runback from upstream is also negligible.

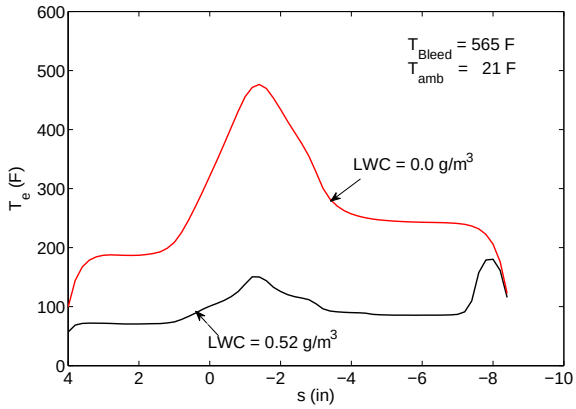

Fig. 17 Face sheet surface temperature distribution ($T_{amb} = 21F$)

The analysis result for $-22°F$ ambient temperature, and $490°F$ bleed air temperature (case-2) for dry ($LWC = 0$) condition and wet ($LWC = 0.14$) condition are shown on Fig. 18. Since both ambient temperature and bleed temperature are lower than the case-1 the dry condition surface temperature distribution is lower than the case-1 dry condition temperature distribution. The case-2 results also show as expected the skin temperature for wet condition is lower than the dry condition due to evaporation of water impinging on the surface. For the wet condition, near the stagnation point region a slightly higher skin temperature is observed as in case-1. Next to the stagnation region, following a dip the temperature gradually increases due to lower LWC (0.14). Both runback water and impinging water evaporation are lower. The case-2 wet condition surface temperature distribution is higher than the case-1 wet condition distribution due to lower LWC specified for case-2.

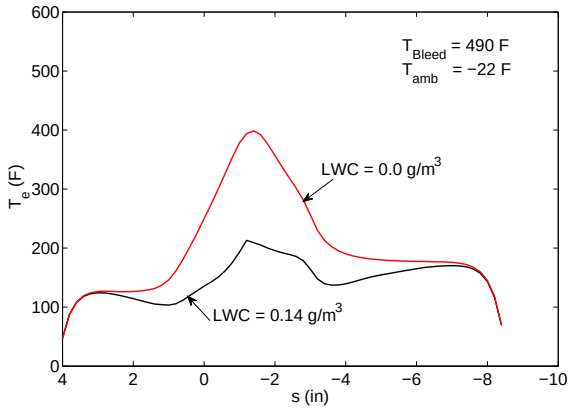

Fig. 18 Face sheet surface temperature distribution ($T_{amb} = -22F$)

6 Acknowledgement

We would like to thank Dr. Kurt Soschinske of Mechanical Engineering Department, Wichita State University (formerly with the Boeing Company), for pointing out the existence of a US Patent [17] and the Japanese transpiration flow research work [9] during the design and development of the acoustically treated nacelle lip.

7 Copyright Statement

References

[1] Birkhoff G, Varga R. S, and Young D. Alternating Direction Implicit Methods. In Alt F and Rubinoff M, editors, *Advances in Computers*, Vol. 3, pp 189–273, New York, 1962. Academic Press.

[2] Boelter L. M. K, Grossman L. M, Martinelli R. C, and Morrin E. H. Investigation of Aircraft Heaters: Comparison of Several Methods of Calculating Heat Losses from Airfoils. NACA TN 1453, 1948.

[3] Breer M. D, Olsen R. F, Kunze, Jr. R. K, and Riedel B. L. U.S. Patent 6,371,411, Method and apparatus for aircraft inlet ice protection, April 2002.

[4] Breer M. D, Olsen R. F, Kunze, Jr. R. K, and Riedel B. L. U.S. Patent 6,457,676, Method and apparatus for aircraft inlet ice protection, April 2002.

[5] Breer M. D, Olsen R. F, Kunze, Jr. R. K, and Riedel B. L. U.S. Patent 6,488,558, Method and apparatus for aircraft inlet ice protection, April 2002.

[6] Elangovan R and Hung K. E. Minimum heating energy requirements of piccolo tube jet impingement thermal anti-icing system. ASME-JSME Paper HT2007-32080, July 2007.

[7] Elangovan R and Olsen R. F. Analysis of layered composite skin electro-thermal anti-icing system. AIAA Paper AIAA-2008-0446, January 2008.

[8] Herkes W. H, Olsen R. F, and Uellenberg S. The quiet technology demonstrator program: Flight validation of airplane noise-reduction concepts. AIAA-2006-2720, 12th AIAA/CEAS Aeroacoustics Conference (27th AIAA Aeroacoustics Conference), May 2006.

[9] Kikkawa S, Senda M, Sakaguchi K, and Shibutani H. Transpiration cooling using air as a coolant. *Trans. Jap. Soc. of Mech. Eng., Part B*, Vol. 57, No 542, pp 3531–3536 (in Japanese), 1991.

[10] Mathews D. C, Bock L. A, Bielak G. W, Dougherty R. P, Premo J. W, Scharpf D. F, and Yu J. Pratt & Whitney/Boeing engine validation of noise reduction concepts. Final NASA Contractor Report for NASA Contract NAS3-97144, Phase 1 (to be published).

[11] Messinger B. L. Equilibrium Temperature of an Unheated Icing Surface as a Function of Air Speed. *Journal of the Aernautical Sciences*, Vol. 20, pp 29–42, January 1953.

[12] Noise Rule a. London Heathrow Noise Rule. URL `http://www.boeing.com` /commercial/noise/heathrow.html.

[13] Noise Rule b. Official Journal of the European Communities, 28.3.2002, Directive 2002/30/EC of the European Parliament and of The Council, of 26 March 2002 on the establishment of rules and procedures with regard to the introduction of noise-related operating restrictions at Community airports.

[14] Noise Rule c. Heathrow Airport, Conditions of Use Including Airport Charges from 1 April 2008, 28 March 2008. URL `http://www.boeing.com`/commercial/noise/ConditionsofUseHeathrow2008.pdf.

[15] Noise Rule d. Courtesy translation from a copy of the "Official Journal of the French Republic" J.O. No. 213 of 14 September 2003, page 15791, Order dated 8 September 2003 concerning the extension of operating restrictions for the noisiest 'Chapter 3' aircraft at the Paris-Charles-de-Gaulle Airport (Val d'Oise). URL `http://www.boeing.com`/commercial/noise/cdgnew.pdf.

[16] Noise Rule e. Chapter 4 Requirements: Applicability for new type designs, January 1, 2006. URL http://www.boeing.com/ commercial/noise/chapter4.pdf.

[17] Parente C. A. U.S. Patent 5,841,079, Combined acoustic and anti-ice engine inlet liner, November 1998.

[18] Peaceman D. W and Rachford, Jr. H. H. The Numerical Solution of Parabolic and Elliptic Differential Equations. *Journal of the SIAM*, Vol. 3, No 1, pp 28–41, March 1955.

[19] Ruff G. A and Berkowitz B. M. Users Manual for the NASA Lewis Ice Accretion Prediction Code (LEWICE). NASA CR 185129, 1990.

[20] Sogin H. H. *A Design Manual for Thermal Anti-icing Systems*. WADC Technical Report 54-313, December 1954.

[21] Yu J, Nesbitt E, Chien E, Uellenberg S, Kwan H, Premo J, Ruiz M, and Czech M. Qtd2

(Quiet technology demonstrator 2) Intake liner design and validation. AIAA-2006-2458, 12th AIAA/CEAS Aeroacoustics Conference (27th AIAA Aeroacoustics Conference), May 2006.